Raman spectroscopy and lattice dynamics calculations of tetragonally-structured single crystal zinc phosphide (Zn$_3$P$_2$) nanowires

Elias Z. Stutz,[1] Simon Escobar Steinvall,[1] Alexander P. Litvinchuk,[2] Jean-Baptiste Leran,[1] Mahdi Zamani,[1] Rajrupa Paul,[1] Anna Fontcuberta i Morral,[1,3] Mirjana Dimitrievska[1]*

1 - Laboratory of Semiconductor Materials, Institute of Materials, Ecole Polytechnique Fédérale de Lausanne, 1015 Lausanne, Switzerland.

2 - Texas Center for Superconductivity and Department of Physics, University of Houston, Houston, Texas 77204-5002, United States of America

3 – Institute of Physics, Ecole Polytechnique Fédérale de Lausanne, 1015 Lausanne, Switzerland

* E-mail: mirjana.dimitrievska@epfl.ch

Abstract

Earth-abundant and low-cost semiconductors, such as zinc phosphide (Zn$_3$P$_2$), are promising candidates for the next generation photovoltaic applications. However, synthesis on commercially available substrates, which favors the formation of defects, and controllable doping are challenging drawbacks that restrain device performance. Better assessment of relevant properties such as structure, crystal quality and defects will allow faster advancement of Zn$_3$P$_2$, and in this sense Raman spectroscopy can play an invaluable role. In order to provide a complete Raman spectrum reference of Zn$_3$P$_2$, this work presents a comprehensive analysis of vibrational properties of tetragonally-structured Zn$_3$P$_2$ (space group $P4_2/nmc$) nanowires, from both experimental and theoretical perspectives. Low-temperature high-resolution Raman polarization measurements have been performed on single-crystalline nanowires. Different polarization configurations have allowed selective enhancement of A$_{1g}$, B$_{1g}$ and E$_g$ Raman modes, while B$_{2g}$ modes were identified from complementary unpolarized Raman measurements. Simultaneous deconvolution of all Raman spectra with Lorentzian curves has allowed identification of 33 peaks which have been assigned to 34 (8 A$_{1g}$ + 9 B$_{1g}$ + 3 B$_{2g}$ + 14 E$_g$) out of the 39 theoretically predicted eigenmodes. The experimental results are in good agreement with the vibrational frequencies that have been computed by first-principles calculations based on density functional theory. Three separate regions were observed in the phonon dispersion diagram: (i) low frequency region (< 210 cm-1) which is dominated by Zn-related vibrations, (ii) intermediate region (210 – 225 cm-1) which represents a true phonon gap with no observed vibrations, and (iii) high frequency region (> 225 cm-1) which is attributed to primarily P-related vibrations. The analysis of vibrational patterns has shown that non-degenerate modes involve mostly atomic motion along the long crystal axis (c-axis), while degenerate modes correspond primarily to in-plane vibrations, perpendicular to the long c-axis. These results provide a detailed reference for identification of the tetragonal Zn$_3$P$_2$ phase, and can be used for building Raman based methodologies for effective defect screening of bulk materials and films, which might contain structural inhomogeneities.

Introduction

Among the II-V compounds, zinc phosphide (α-Zn$_3$P$_2$, hereafter referred to as Zn$_3$P$_2$), an earth-abundant, environmentally friendly and low-cost semiconductor, has gained attention as a promising absorber candidate for the next generation of thin film photovoltaics (PV) [1–3]. With merits such as a direct band gap of 1.5 eV, high absorption coefficient of 10^4 - 10^5 cm^{-1}, and carrier diffusion lengths of ~10 μm, zinc phosphide is a very suitable material for solar energy applications [4–9]. However, even with

all these benefits, the conversion efficiencies are still far from reaching the 31% predicted from the Shockley−Queisser limit[10]. In fact, the record solar cell, with a conversion efficiency of ~6%, was produced 40 years ago[11], and since then there has not been any significant scientific breakthrough. Despite the highly promising result at that time, research on Zn_3P_2 recessed mostly due to technical challenges in fabricating high-quality material with controllable doping, surface passivation and clean interfaces, all of which are crucial for high efficiency devices.

One major challenge in the synthesis of high quality Zn_3P_2 is its rather large crystallographic unit cell [11] when compared to other PV materials, along with its high coefficient of thermal expansion[13,14]. All of these increase heterointerface defect densities when grown epitaxially on commercially available substrates. A major progress has recently been made in this regard, where growth of highly crystalline Zn_3P_2 was achieved using innovative nanofabrication methods (i.e. selective area epitaxy) [15–17]. However, fine tuning of the material's functional properties through doping and defect engineering still remains a challenge. This is mostly due to the complex structure of Zn_3P_2 characterized by empty sites in the cubic zinc sublattice dispersed throughout a tetragonal lattice, which, besides providing ample opportunities for material design, also results in a higher probability for formation of intrinsic defects during synthesis (i.e. phosphorus interstitials in the empty zinc sites). While some amounts of intrinsic defects are beneficial for the doping and recombination characteristics of the Zn_3P_2, large concentrations of defect complexes can lead to limiting minority charge carrier lifetimes and enhance recombination processes[6,18,19]. Defects can also have an effect on the net band gap variations and cause localized band gap or electrostatic potential fluctuations, which can lead to change in the bulk diffusivity and indirectly affect the optoelectronic properties.[19,20] This is why controlled defect engineering and doping play a significant role in achieving high efficiency devices based on Zn_3P_2. Thus, a thorough assessment of Zn_3P_2, in terms of crystalline quality, defect identification and quantification, and homogeneity, is of the foremost importance for future development of this technology. In particular, developing predictive synthesis–structure–property relationships are crucial for effective design of materials with enhanced functional properties as absorbers for high efficiency devices.

Raman spectroscopy can play an important role in this context. Besides being a fast and non-destructive technique, it is also one of the most suitable tools for determining crystal structure and quality of semiconductors. This is due to the intensity, shape and position of Raman peaks being strongly influenced by the presence of structural inhomogeneities in the material. These include both point defects, such as vacancies, interstitials, and anti-sites, and other structural disorders, like dislocations or grain boundaries. Clear variations in Raman spectral features with the changes in the composition, processing conditions and doping can be observed for many materials[21–27]. However, in order to be able to use Raman spectroscopy as a suitable tool for defect identification, it is necessary to have reliable reference Raman spectra of the material, with detailed identification of all peaks and their vibrational origin. This can greatly help in building Raman based methodologies which can be later used for further development of materials in the PV field.

In this work we provide a reference Raman spectrum of single crystalline Zn_3P_2, with a complete analysis of all Raman active modes from both experimental and theoretical perspectives. To the best of our knowledge, this is the first comprehensive theoretical analysis of the lattice vibrations in Zn_3P_2 along with a concise comparison with experimental results in terms of phonon symmetries and frequencies. So far, the most complete experimental Raman analysis of Zn_3P_2 was performed by Pangilinan et al. (Ref. [28]). However, this work contained a few inconsistencies in terms of the number of observed modes and their symmetry assignment. Later on, Hanuza et al. provided data on the vibrational modes in zinc phosphide by reflectance spectroscopy [29]. The identification of the modes was supported by a molecular model of a simplified Zn_3P_2 structure with 18 atoms out of the 40 present

in the Zn_3P_2 unit cell, which resulted in a somehow qualitative assessment of the vibrations in the structure. On the other hand, density functional theory (DFT) calculations of Zn_3P_2 have primary been dealing with the prediction of the electronic band structure[30], defects[31,32] and growth mechanisms[33,34], rather than the phonon analysis.

This work provides high resolution polarization resolved Raman scattering measurements. The experiments have been performed on the basal (010) plane of single crystal nanowires in high-symmetry polarization conditions. Together with the detailed deconvolution of the Raman spectra with Lorentzian curves, this has allowed the identification of 33 Raman peaks. The experimental results are consistent with the vibrational frequencies that have been computed by first-principles calculations based on DFT. Furthermore, calculations of the phonon density of states (PDOS) (elemental and total), as well as the phonon dispersions provide a microscopic understanding of the experimentally observed phonon lines, in addition to the assignment to the specific lattice eigenmodes. These results can be used as a reference for identification of the Zn_3P_2 phase, as well as for building Raman based methodologies for effective defect screening of bulk materials and films that might contain structural inhomogeneities.

Experimental details

Material preparation. The Zn_3P_2 nanowires were epitaxially grown in a Veeco GENxplor molecular beam epitaxy (MBE) system on InP (100) substrates. They were grown via a In-catalysed vapour-liquid-solid method. The In was generated through a 5-minute Zn pre-deposition prior to growth, which reacted with the substrate to form the catalyst droplet. The analyzed samples were then grown at a manipulator temperature of 250°C and a P/Zn ratio of 1.45 for four hours (Zn base flux 3.4×10^{-7} Torr). Additional details on the growth can be found in Ref. [15,35].

Characterization. The morphological properties of the nanowires were characterized by scanning electron microscopy (SEM) with a Zeiss Merlin microscope operated at 3 kV. (Scanning) Transmission electron microscopy (S/TEM) and energy dispersive x-ray spectroscopy (EDX) studies were performed using an FEI Talos transmission electron microscope operating at 200 kV. For TEM analysis, the nanowires were transferred to a copper grid covered by holey-carbon by gently scraping it across the substrate surface with a cotton swab.

Micro-Raman spectroscopy was realized in the backscattering configuration on a Zn_3P_2 nanowire at 12 K. The 532 nm line of a Coherent Sapphire SF optically pumped semiconductor laser was used for excitation. The beam was focused on the sample with a microscope objective with a numerical aperture of 0.75, resulting in around 1 µm diameter spot size, and reached radiant fluxes on the order of 150 µW at the surface. A linear polarizer and a half-waveplate were used to control the polarization of the incident beam, while the scattered light was filtered through a linear polarizer. Before entering the spectrometer, a half-waveplate oriented the light polarization parallel to the entrance slit. The signal was analyzed with a TriVista triple spectrometer with 900 mm^{-1}, 900 mm^{-1} and 1800 mm^{-1} gratings in subtractive mode and a Princeton Instruments liquid nitrogen cooled multichannel CCD PyLoN camera. The polarization direction is described by the angle it makes with the direction of the long axis of the nanowire. For Raman analysis, the nanowires were transferred to a silicon wafer by gently brushing the growth substrate against it.

Lattice Dynamics Calculations. The first-principles calculations of the electronic ground state of the tetragonally structured Zn_3P_2 were performed within the local density approximation (LDA) using Ceperly-Adler functional [36,37], as implemented in the CASTEP code[38]. Norm-conserving pseudopotentials were used. The cutoff energy for the plane wave basis was set to 600 eV. A self-

consistent-field (SCF) tolerance better than 10^{-7} eV per atom and the phonon SCF threshold of 10^{-12} eV per atom were imposed. Prior to performing calculations, the structure was relaxed so that forces on atoms in the equilibrium position did not exceed 2 meV Å^{-1} and the residual stress was below 5 MPa. Experimentally determined lattice parameters from Ref.[12] were used as a starting point. An integration over the Brillouin zone was performed over a 3 × 3 × 2 Monkhorst−Pack grid in reciprocal space.

Results and discussion

A sketch of the crystal structure of Zn_3P_2 is depicted in Figure 1. It exhibits tetragonal symmetry with the space group $P4_2/nmc$ (D_{4h}^{15}), which contains 8 formula units, resulting in total of 40 atoms per unit cell. The packing of atoms in the structure takes place in a layered lattice along the [001] direction (c-axis), with alternating layers of cations (Zn) and anions (P). The cations are placed at four nearly equidistant planes occupying three distinct $8g$ (1/4, y, z) symmetry positions. The anions are located between the cation planes, with P atoms occupying three inequivalent Wyckoff positions at $4c$ (-1/4, 1/4, z), $4d$ (-1/4, 1/4, z) and $8f$ (x, -x, 1/4). The Zn and P atoms form a tetrahedral arrangement like in zinc-blende and fluorite type structures. Based on this arrangement P atoms form a face-centered cubic sublattice with Zn atoms filling 3/4 of the tetrahedral voids. Each P atom is surrounded by 6 Zn atoms at the corners of a distorted cube while the metal atoms are surrounded by 4 P atoms at the vertices of a distorted tetrahedron. The ordered unoccupied tetrahedral voids lead to a decrease in lattice symmetry and the significant extension of Zn_3P_2 unit cell when compared to the zinc-blende or fluorite building blocks. The experimentally determined lattice parameters are $a = b = 8.0785$ Å and $c = 11.3966$ Å [12].
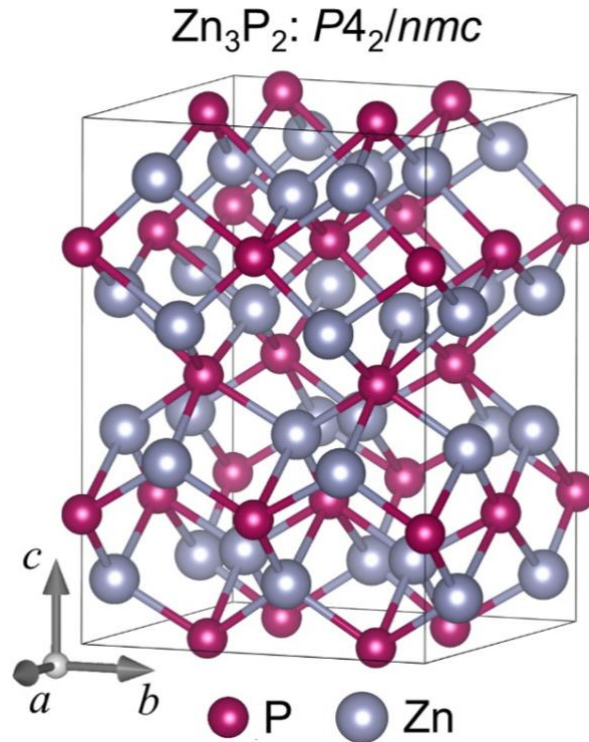

Figure 1. Conventional unit cell representation of the tetragonal Zn_3P_2 structure.

4

Group theory analysis predicts the following set of irreducible representation for the structure $P4_2/nmc$ (D_{4h}^{15}) at the Γ point of the Brillouin zone [39–41]:

$$\Gamma_{total} = 9A_{1g} + 5A_{2g} + 10B_{1g} + 4B_{2g} + 16E_g + 4A_{1u} + 10A_{2u} + 5B_{1u} + 9B_{2u} + 16E_u,$$

from which the Raman and infra-red (IR) active modes are:

$$\Gamma_{Raman} = 9A_{1g} + 10B_{1g} + 4B_{2g} + 16E_g,$$

$$\Gamma_{IR} = 9A_{2u} + 15E_u,$$

while the other modes are silent. Note also that the A and B modes are non-degenerate, while the E modes are doubly degenerate. The Raman tensors for $P4_2/nmc$ space group are defined as follows:

$$\mathfrak{R}_{A_{1g}} = \begin{pmatrix} a & 0 & 0 \\ 0 & a & 0 \\ 0 & 0 & b \end{pmatrix}; \; \mathfrak{R}_{B_{1g}} = \begin{pmatrix} c & 0 & 0 \\ 0 & -c & 0 \\ 0 & 0 & 0 \end{pmatrix}; \; \mathfrak{R}_{B_{2g}} = \begin{pmatrix} 0 & d & 0 \\ d & 0 & 0 \\ 0 & 0 & 0 \end{pmatrix}; \; \mathfrak{R}_{E_g} = \begin{pmatrix} 0 & 0 & e \\ 0 & 0 & e \\ e & e & 0 \end{pmatrix} \quad (1)$$

where a, b, c, d, and e are the Raman tensor elements.

In order to experimentally determine the positions of the Raman active modes, high-resolution Raman polarization measurements were performed on a Zn_3P_2 nanowire, of which SEM micrographs are presented in Figure 2. The nanowires present a square cross-section that decreases in area along the nanowire axis. At the top we find the indium droplet that catalyzes the growth. The Raman measurements were carried out at approximately one third of the length of the nanowire from the wide base. The nanowire width being at least 100 nm wide along the whole structure and more than 600 nm wide at the location of the measurement.Consequently, phonon confinement effects are negligible, and the measured spectrum is equivalent to that of the bulk material.
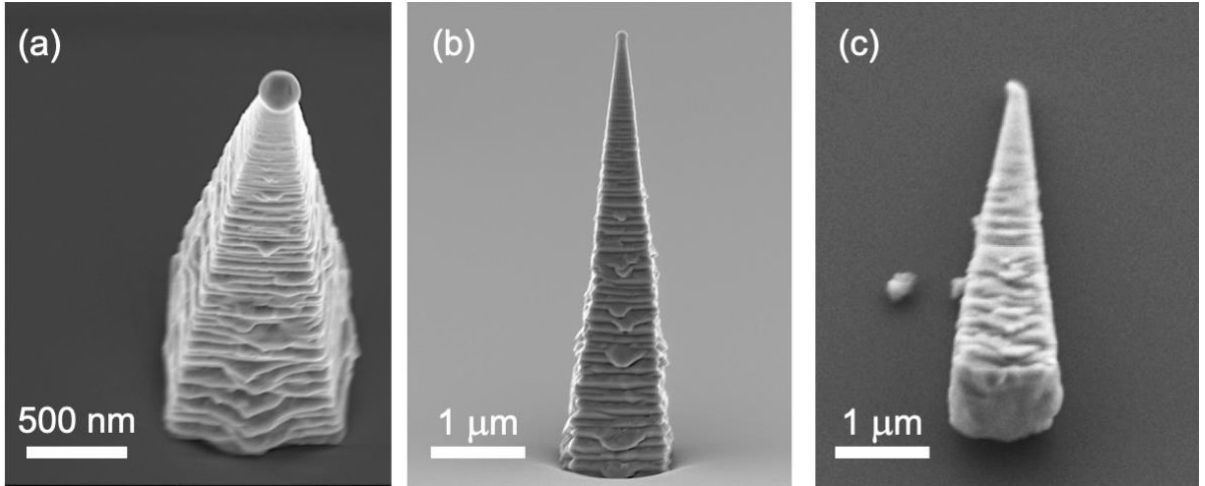

Figure 2. SEM micrographs of three different Zn_3P_2 nanowires grown vertically along the [001] direction. The images are taken in different configurations, with the nanowire orientation being (a) and (b) perpendicular and (c) parallel to the substrate (transferred for the optical measurements). The Raman spectra presented in this study were acquired from the wire shown in (c).

Selective area electron diffraction measurements on the nanowires in TEM have confirmed formation of monocrystalline Zn_3P_2 phase with $P4_2/nmc$ tetragonal symmetry, and allowed identification of the nanowire growth orientation as [001], with the c crystal axis perpendicular to the substrate [15]. It should be noted that the roughness on the nanowire surface is not due to crystallographic defects but

rather microfaceting as the (101) facets have a lower surface energy than (100) facets, and thus the surface has the same crystalline orientation as the core of the nanowire and does not affect the Raman spectrum. The compositional assessment, performed by STEM-EDX, indicated the formation of Zn-rich wires with Zn/P = 2.3 compared to stochiometric Zn/P = 1.5. The extra Zn is probably accommodated at the empty Zn sites in the lattice, and therefore it should not affect the positions of the main Raman modes expected for this crystal structure. Further, a homogenous distribution of Zn and P with no phase segregation is observed from the compositional maps shown in Figure 3. This confirms that only peaks from the Zn_3P_2 phase are expected in the Raman spectra.
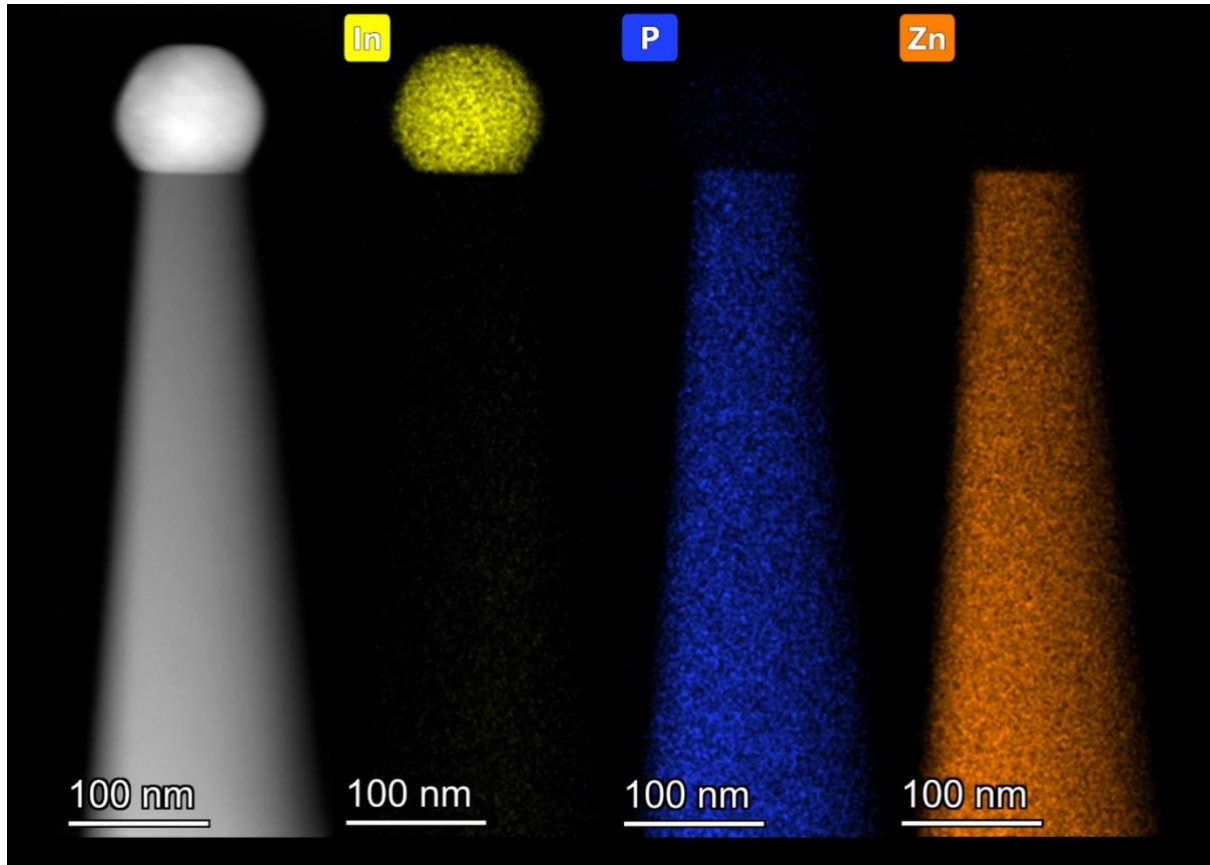

Figure 3. High-angle annular dark-field STEM image and accompanying EDX elemental maps of the top of a Zn_3P_2 nanowire with composition corresponding to Zn/P = 2.3.

Raman measurements were performed on a nanowire with the [001] growth direction being parallel to the substrate (Figure 2(c)), indicating (010) crystallographic plane as the basal plane.

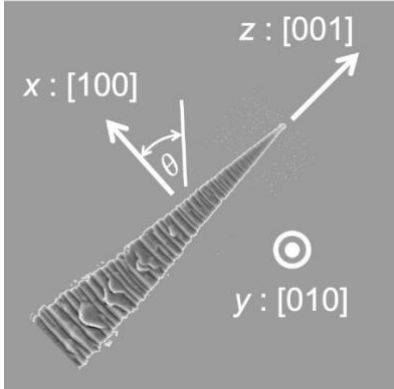Based on these conditions, the angular dependence of the Raman mode intensity is given by:

$$I \propto \left| v_i \, \Re_{xyz} \, v_s \right|^2, \tag{2}$$

$$v_i = (\cos\theta \quad 0 \quad \sin\theta); \quad v_s^{\parallel} = \begin{pmatrix} \cos\theta \\ 0 \\ \sin\theta \end{pmatrix}; \quad v_s^{\perp} = \begin{pmatrix} -\sin\theta \\ 0 \\ \cos\theta \end{pmatrix}, \tag{3}$$

where v_i and v_s are the unit polarization vectors of the electric field for the incident and scattered light, respectively, and $\Re_{xyz}$ is the Raman tensor, while θ is the angle between the [100] nanowire direction and the electric filed of the incident light. The superscripts ∥ and ⊥ correspond to the parallel and

perpendicular polarization configurations. Substitution of Raman tensors from Eq. (1) into Eq. (2) and (3) yields general angular dependencies of the intensities of the Raman modes, which are presented in Table 1.

Table 1. Angular dependencies of Raman modes intensity for tetragonal Zn_3P_2 in case of a (010) basal plane, and with the incident and scattered light parallel to the [010] direction.

Polarization geometry	Mode	Parallel configuration	Perpendicular configuration
	A_{1g}	$\lvert a (\cos \theta)^2 + b (\sin \theta)^2 \rvert^2$	$\left\lvert \frac{1}{2}(b-a)\sin 2\theta \right\rvert^2$
	B_{1g}	$\lvert c (\cos \theta)^2 \rvert^2$	$\left\lvert -\frac{1}{2}c \sin 2\theta \right\rvert^2$
	B_{2g}	0	0
	E_g	$\lvert e (\sin 2\theta)^2 \rvert^2$	$\lvert e (\cos 2\theta)^2 \rvert^2$

Based on the angular dependencies of Raman modes intensity from Table 1, three polarization geometry configurations were chosen for selective activation of specific phonon symmetries in the Raman spectra, thus allowing easier identification of the peak characteristics. The chosen polarization geometries correspond to the maximum or minimum Raman response of the lattice, in terms of the A_{1g}, B_{1g} and E_g modes. Raman measurements in parallel configuration with $\theta = 90°$ allow selective enhancement of only the A_{1g} modes, while for $\theta = 0°$ both A_{1g} and B_{1g} modes are expected. On the other side, polarization measurements in the perpendicular configuration with $\theta = 90°$ will selectively enhance only the E_g modes. Finally, unpolarized Raman measurements were performed in order to identify B_{2g} vibrations.

Figure 4 presents the Raman spectra of Zn_3P_2 measured at 12 K under different polarization configurations using 532 nm excitation. Low temperature measurements were chosen due to the increase in the phonon lifetime in the material, which results in better defined Raman peaks. This allows for a repeatable and reliable spectrum deconvolution as it decreases the overlap between Raman lines. The standard Porto notation has been utilized for labeling of the measurements, where $< -Y|ZX|Y >$ denotes the incoming radiation along the -y-axis being polarized along the z-axis with the backscattered (y) light polarized along x. It should be noted that in case of the $< -Y|ZX|Y >$ polarization configuration, besides the allowed E_g modes, appearance of extra peaks is observed with closely matching positions and characteristics of A_{1g} modes. The activation of forbidden A_{1g} modes under this measurement geometry can be explained by possible breakdown of selection rules. For example, planar native defects in the form of stacking faults with the direction of growth in the c axis, which are often found in layered materials due to very low formation energy, could activate forbidden modes [26,42–44]. Additionally, breakdown of selection rules can activated by the photonic nature of the light–nanowire interaction, which can modify the light polarization inside the nanowire[45–48].

Raman spectra were deconvoluted with a minimum number of Lorentzian components, allowing identification of a total of 33 peaks from the four different Raman measurement configurations. A representative deconvolution of the Raman spectra of Zn_3P_2, along with details regarding the deconvolution procedure and identification of the peaks can be found in Supporting Information. It should be noted that all linewidths of the peaks are narrow and similar in values, pointing to their nature as one-phonon modes. Table 2 lists the Raman frequencies of all peaks obtained from the deconvolution, the symmetry assignment based on the polarization conditions, comparison with calculated phonon modes, as well as previously reported experimental results[28]. Table 2 indicates an excellent

agreement (within 2% difference) between the experimentally observed peaks and the theoretically predicted Raman frequencies. Minor disagreement in the Raman peak positions between the experimental and the theoretical results is expected, due to approximations applied during the calculations.

While the peak positions have shown excellent agreement between this work and the results reported in the literature, we would like to point out to several inconsistencies regarding their symmetry assignment. In particular 9 modes out of 26 modes from Ref.[28] do not match the proposed symmetry assignment with the identification performed in this work. These peaks are highlighted in Table 2 by providing the literature's symmetry assignment in parenthesis next to the peak position. One possible reason for the mismatch could be closeness in peak position for different types of modes, which, along with some breakdown in selection rules due to the defects present in the crystal, as reported in Ref. [28], could result in the appearance of forbidden modes in the Raman spectra, and consequently lead to misinterpretation. Additionally, we also point out that the proposed mode assignment in Ref. [28] is based solely on experimental results, while this work is supported by both theoretical calculations and polarization measurements.
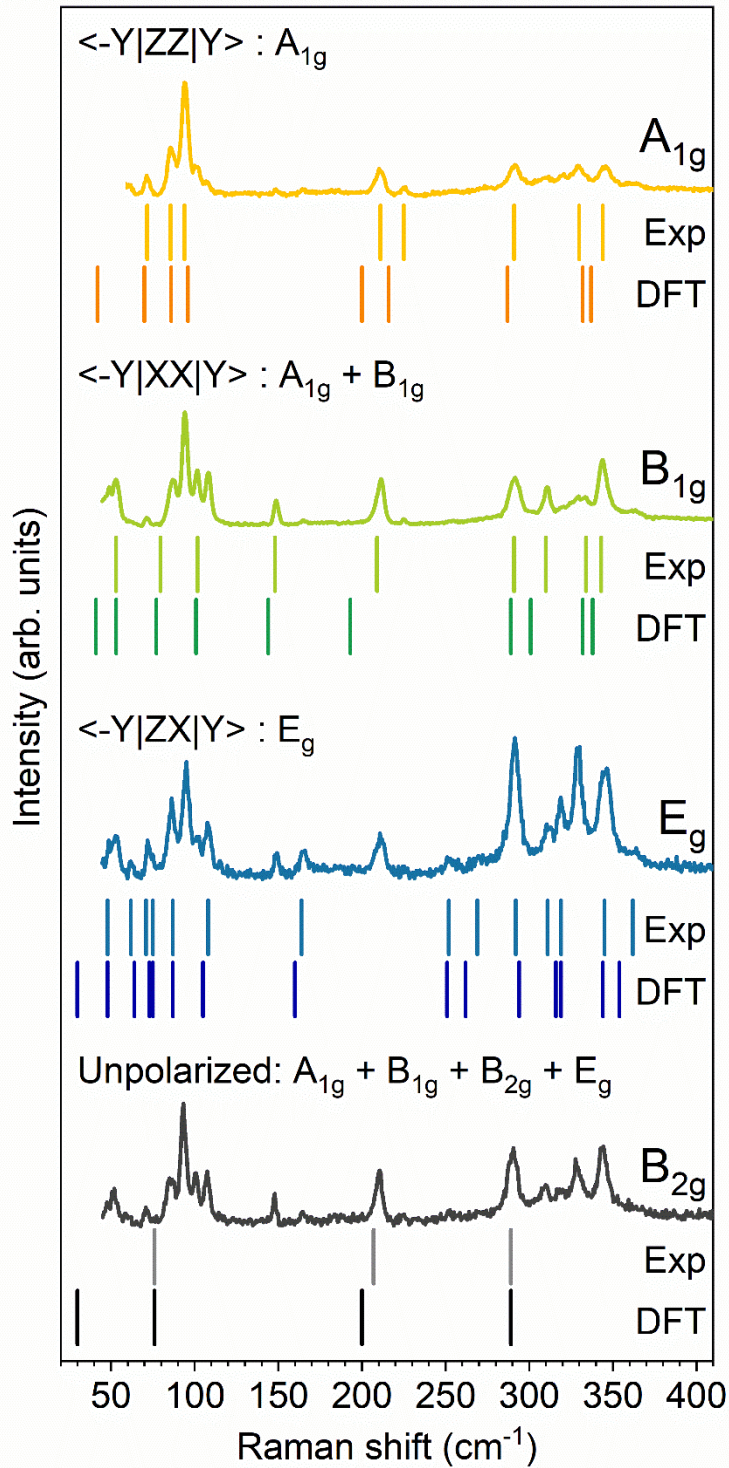
Figure 4. Raman spectra of Zn_3P_2 in polarized and unpolarized configurations measured at 12 K using 532 nm excitation wavelength. The polarization geometry is indicated above each spectrum, along with the labels of the specific phonons that are allowed in these conditions. The lines under each spectrum show comparison between the Raman peak positions obtained experimentally by the deconvolution of the spectra with Lorentzian curves (labeled Exp), and from the lattice dynamics calculations based on DFT (labeled DFT).

Table 2. Frequency (in cm^{-1}) of peaks from Lorentzian fitting of Raman spectra measured with 532 nm and proposed mode symmetry assignment compared with theoretical predictions and reported experimental data from literature.

This work			Reference[28]
ν_{exp} (cm^{-1})	ν_{theory} (cm^{-1})	Symmetry assignment	ν_{exp} (cm^{-1})
	14	E_g	
	30	B_{2g}	
	30	E_g	
	41	B_{1g}	41 (E_g)
	42	A_{1g}	
48	48	E_g	48 (B_{2g})
53	53	B_{1g}	53 (A_{1g})
62	64	E_g	62
71	70	A_{1g}	
72	73	E_g	71
75	75	E_g	
76	76	B_{2g}	
79	77	B_{1g}	
86	86	A_{1g}	87
87	87	E_g	88 (B_{1g})
94	96	A_{1g}	94
102	101	B_{1g}	101 (A_{1g})
108	105	E_g	108 (B_{1g})
148	144	B_{1g}	148
164	160	E_g	164
209	193	B_{1g}	
207	200	B_{2g}	
211	200	A_{1g}	210
225	216	A_{1g}	225
252	251	E_g	251
269	262	E_g	
291	287	A_{1g}	290
289	289	B_{1g}	292
	289	B_{2g}	
292	294	E_g	
309	301	B_{1g}	309
311	316	E_g	310 (A_{1g})
319	319	E_g	319
330	332	A_{1g}	323
334	332	B_{1g}	329 (E_g)
344	337	A_{1g}	333
343	338	B_{1g}	344
345	344	E_g	346
362	354	E_g	362 (A_{1g})

More detailed analysis of the Zn_3P_2 phonons can be obtained from the calculated phonon dispersion along high symmetry directions of the Brillouin zone, which is presented in Figure 5, along with the total and elemental PDOS. Three separate regions can be identified in the phonon dispersion diagram: (i) a low frequency region (< 210 cm^{-1}) which is dominated by Zn-related vibrations, (ii) an intermediate region ($210 - 225$ cm^{-1}) which represents a true phonon gap with no observed vibrations, and (iii) a high frequency region (> 225 cm^{-1}) which is attributed mainly to P-related vibrations. The observation of the phonon gaps seems typical for II-V compounds, as similar features were observed for ZnP_2 and CdP_2 [49]. Additionally, it was noted that the position and shape across the Brillouin zone of those phonon bandgaps seems virtually independent on the cations (Zn or Cd). This feature could be further exploited for thermoelectric applications, for example. It is also important to point out that the tetragonal Zn_3P_2 does not possess any optical phonons above 365 cm^{-1}. This is the consequence of Zn_3P_2 being structurally more similar to ternary and quaternary chalcogenides where anions, similar to cations, are all tetrahedrally coordinated [24,27,50].
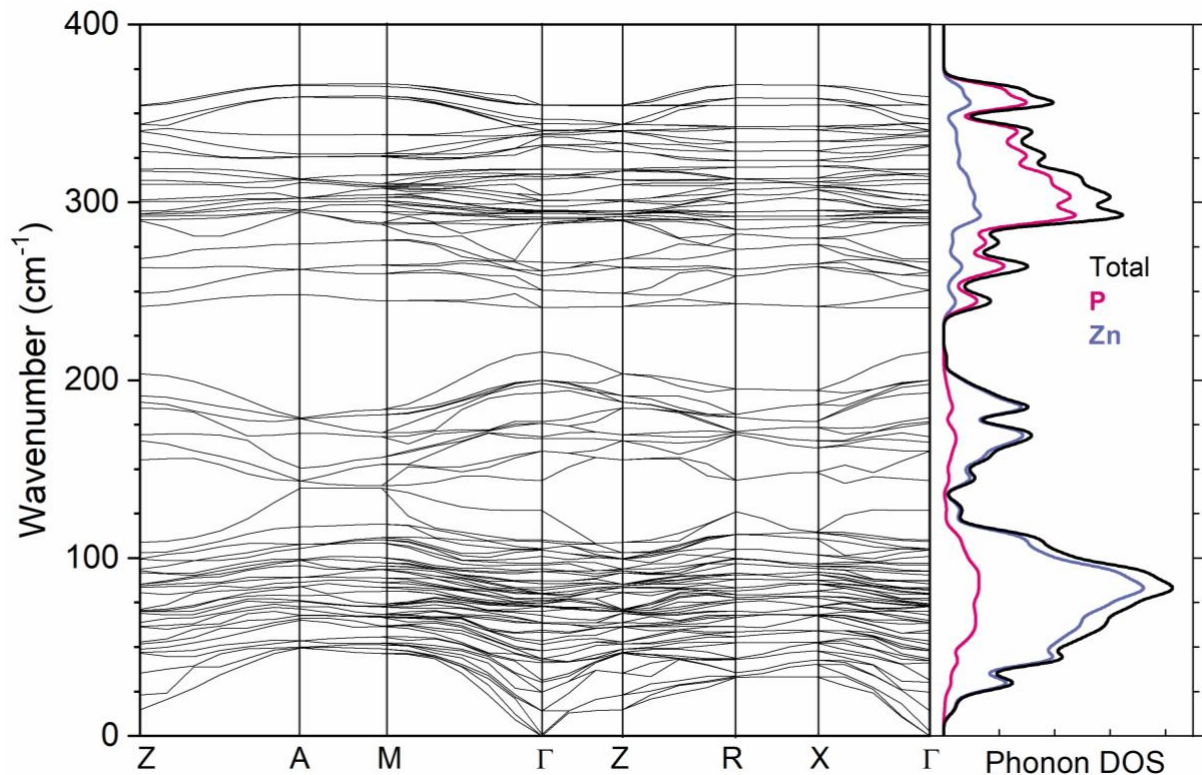

Figure 5. DFT-calculated phonon dispersion along high-symmetry directions of the tetragonal Zn_3P_2 structure. On the right the partial phonon density of states is presented: zinc atoms in blue-gray, phosphorous in pink, and total in black.

Finally, atomic displacements of the Raman modes were calculated to provide the visualization of the corresponding atom motions. Figure 6 shows representative vibrational patterns. As expected from the PDOS, the vibrational patterns are mostly dominated by either Zn (< 200 cm^{-1}) or P motions (> 225 cm^{-1}). E_g-symmetry modes represent primarily in-plane vibrations, perpendicular to the long c-axis of the crystal lattice (160, 316 and 344 cm^{-1}). On the other hand, non-degenerate modes involve mostly atomic motion along the c-axis. A_{1g} mode centered at 200 cm^{-1}, for example, corresponds to compression of Zn layers towards P atoms at $4c$ and $4d$ Wyckoff positions. A_{1g} mode at 287 cm^{-1} involves breathing-like vibrations of P atoms around the vacancy at $8e$ Wyckoff position. On the other hand, A_{1g} mode at 337 cm^{-1} involves asymmetric stretching vibrations along the c crystal axis of P atoms at $4c$ and $4d$ positions. Other modes exhibit more complicated vibrational patterns, which can involve both in and out of plane motions of atoms, as shown in Figure 6.
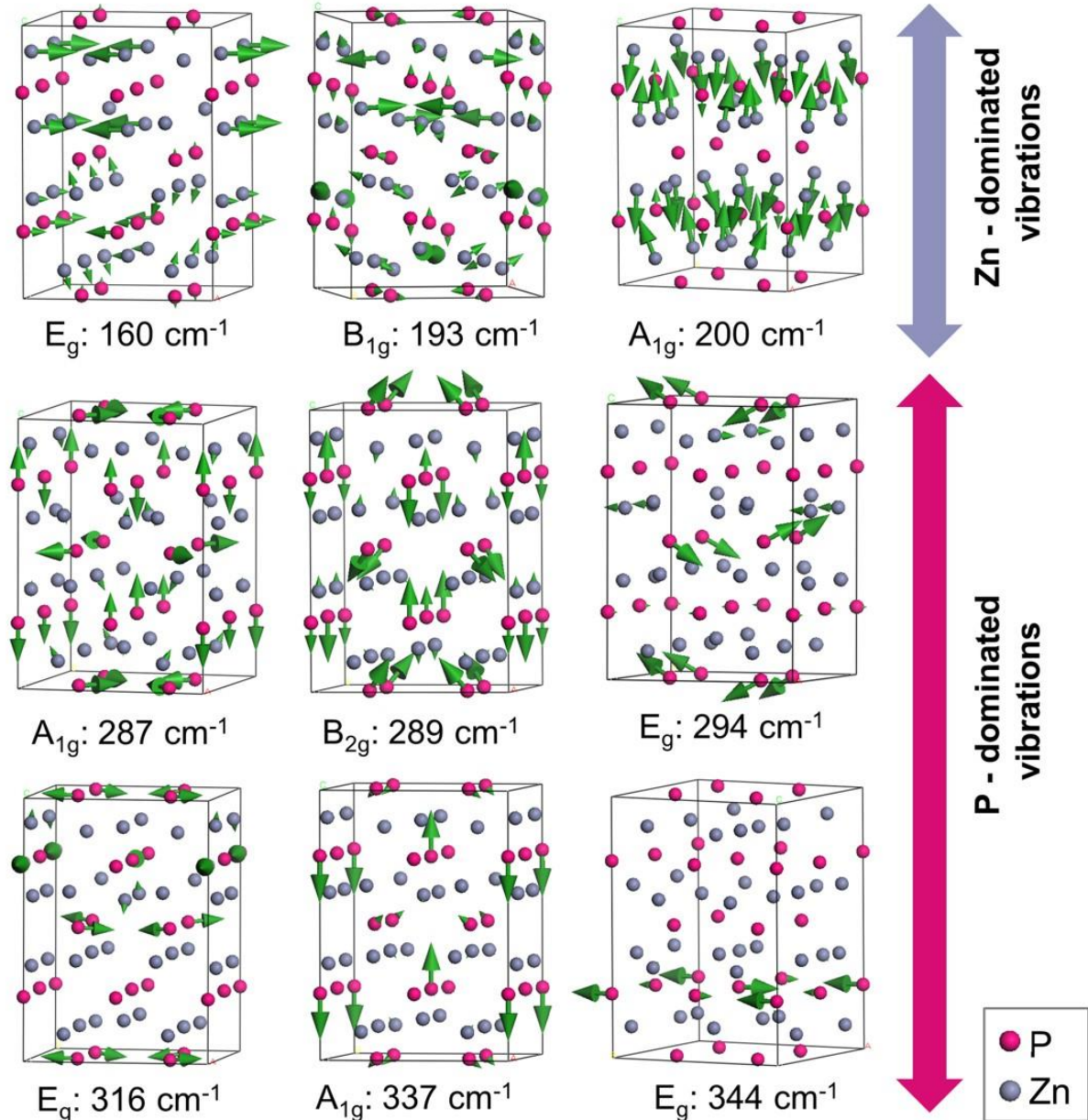
Figure 6. Calculated phonon displacements for several representative modes of Zn₃P₂. Mode symmetries and frequencies (in cm^{-1}) are listed under each picture.

Conclusions

In conclusion, this work provides a reference Raman spectrum of tetragonally-structured Zn₃P₂, with the complete analysis of all Raman active modes from both experimental and theoretical perspective. High resolution Raman scattering measurements that were performed under different polarization configurations on the basal (010) plane of single crystal nanowires, together with the detailed deconvolution of the Raman spectra with Lorentzian curves, have allowed identification of 33 Raman peaks out of 39 even parity vibrational modes. The experimental results are in good agreement with the vibrational frequencies that have been computed by first-principles calculations based on DFT. Further calculations of the PDOS (elemental and total), as well as the phonon dispersions allowed better understanding of the experimentally observed phonon lines, as well as the assignment to the specific lattice eigenmodes. In particular, three separate regions were observed in the phonon dispersion diagram: (i) a low frequency region (< 210 cm^{-1}) which is dominated by Zn-related vibrations, (ii) an

intermediate region (210 – 225 cm^{-1}) which represents a true phonon gap with no observed vibrations, and (iii) a high frequency region (> 225 cm^{-1}) which is attributed to primarily P-related vibrations. These results can be used as a reference for identification of the Zn$_3$P$_2$ phase, as well as for building Raman based methodologies for effective defect screening of bulk materials and films, which might contain structural inhomogeneities.

Acknowledgements

References

[1]   Wadia C, Alivisatos A P and Kammen D M 2009 Materials Availability Expands the Opportunity for Large-Scale Photovoltaics Deployment *Environ. Sci. Technol.* **43** 2072–7

[2]   Misiewicz J, Bryja L, Jezierski K, Szatkowski J, Mirowska N, Gumienny Z and Placzek-Popko E 1994 Zn$_3$P$_2$—a new material for optoelectronic devices *Microelectronics Journal* **25** xxiii–xxviii

[3]   Ehrler B, Alarcón-Lladó E, Tabernig S W, Veeken T, Garnett E C and Polman A 2020 Photovoltaics Reaching for the Shockley–Queisser Limit *ACS Energy Lett.* **5** 3029–33

[4]   Swinkels M Y, Campo A, Vakulov D, Kim W, Gagliano L, Escobar Steinvall S , Detz H, De Luca M, Lugstein A, Bakkers E, Fontcuberta i Morral A and Zardo I 2020 Measuring the Optical Absorption of Single Nanowires *Phys. Rev. Applied* **14** 024045

[5]   Pawlikowski J M 1981 Band structure and properties of Zn$_3$P$_2$— promising new infrared material∗ *Infrared Physics* **21** 181–7

[6]   Briones F, Wang F and Bube R H 1981 Pair transitions in Zn$_3$P$_2$ *Appl. Phys. Lett.* **39** 805–7

[7]   Kimball G M, Müller A M, Lewis N S and Atwater H A 2009 Photoluminescence-based measurements of the energy gap and diffusion length of Zn$_3$P$_2$ *Appl. Phys. Lett.* **95** 112103

[8]   Convers Wyeth N and Catalano A 1979 Spectral response measurements of minority-carrier diffusion length in Zn$_3$P$_2$ *Journal of Applied Physics* **50** 1403–7

[9]   Misiewicz J 1990 Inter-band transitions in Zn3P2 *J. Phys.: Condens. Matter* **2** 2053–2072

[10]   Shockley W and Queisser H J 1961 Detailed Balance Limit of Efficiency of p-n Junction Solar Cells *Journal of Applied Physics* **32** 510–9

[11]   Bhushan M and Catalano A 1981 Polycrystalline Zn$_3$P$_2$ Schottky barrier solar cells *Appl. Phys. Lett.* **38** 39–41

[12]   Zanin I E, Aleinikova K B, Afanasiev M M and Antipin M Yu 2004 Structure of Zn$_3$P$_2$ *J Struct Chem* **45** 844–8

[13]   Long J 1983 The Growth of Zn$_3$P$_2$ by Metalorganic Chemical Vapor Deposition *J. Electrochem. Soc.* **130** 725

[14]   Chu T L, Chu S S, Murthy K, Stokes E D and Russell P E 1983 Deposition and properties of zinc phosphide films *Journal of Applied Physics* **54** 2063–8

[15]   Escobar Steinvall S, Tappy N, Ghasemi M, Zamani R R, LaGrange T, Stutz E Z, Leran J-B, Zamani M, Paul R and Fontcuberta i Morral A 2020 Multiple morphologies and functionality of nanowires made from earth-abundant zinc phosphide *Nanoscale Horizons* **5** 274–82

[16]   Paul R, Humblot N, Escobar Steinvall S , Stutz E Z, Joglekar S S, Leran J-B, Zamani M, Cayron C, Logé R, del Aguila A G, Xiong Q and Fontcuberta i Morral A 2020 van der Waals Epitaxy of Earth-Abundant Zn_3P_2 on Graphene for Photovoltaics *Crystal Growth & Design* **20** 3816–25

[17]   S. Escobar Steinvall, E. Z. Stutz, R. Paul, M. Zamani, N. Y. Dzade, V. Piazza, M. Friedl, V. de Mestral, J. B. Leran, R. R. Zamani, A. Fontcuberta i Morral, Selective area overgrowth epitaxy of zinc phosphide: an earth-abundant material for photovoltaics, under review.

[18]   Catalano A and Hall R B 1980 Defect dominated conductivity in Zn_3P_2 *Journal of Physics and Chemistry of Solids* **41** 635–40

[19]   Mirowska N and Misiewicz J 1992 Defect-related transitions in Zn_3P_2 studied by means of photovoltaic effect spectroscopy *Semicond. Sci. Technol.* **7** 1332–1336

[20]   Nayak A and Rao D R 1993 Photoluminescence spectra of Zn_3P_2 -Cd_3P_2 thin films *Appl. Phys. Lett.* **63** 592–3

[21]   Panpech P, Vijarnwannaluk S, Sanorpim S, Ono W, Nakajima F, Katayama R and Onabe K 2007 Correlation between Raman intensity of the N-related local vibrational mode and N content in GaAsN strained layers grown by MOVPE *Journal of Crystal Growth* **298** 107–10

[22]   Kazemi-Zanjani N, Kergrene E, Liu L, Sham T-K and Lagugné-Labarthet F 2013 Tip-Enhanced Raman Imaging and Nano Spectroscopy of Etched Silicon Nanowires *Sensors* **13** 12744–59

[23]   Cançado L G, Jorio A, Ferreira E H M, Stavale F, Achete C A, Capaz R B, Moutinho M V O, Lombardo A, Kulmala T S and Ferrari A C 2011 Quantifying Defects in Graphene via Raman Spectroscopy at Different Excitation Energies *Nano Lett.* **11** 3190–6

[24]   Dimitrievska M, Oliva F, Guc M, Giraldo S, Saucedo E, Pérez-Rodríguez A and Izquierdo-Roca V 2019 Defect characterisation in $Cu_2ZnSnSe_4$ kesterites via resonance Raman spectroscopy and the impact on optoelectronic solar cell properties *J. Mater. Chem. A* **7** 13293–304

[25]   Dimitrievska M, Fairbrother A, Pérez-Rodríguez A, Saucedo E and Izquierdo-Roca V 2014 Raman scattering crystalline assessment of polycrystalline Cu_2ZnSnS_4 thin films for sustainable photovoltaic technologies: Phonon confinement model *Acta Materialia* **70** 272–80

[26]   Placidi M, Dimitrievska M, Izquierdo-Roca V, Fontané X, Castellanos-Gomez A, Pérez-Tomás A, Mestres N, Espindola-Rodriguez M, López-Marino S, Neuschitzer M, Bermudez V, Yaremko A and Pérez-Rodríguez A 2015 Multiwavelength excitation Raman scattering analysis of bulk and two-dimensional MoS_2 : vibrational properties of atomically thin MoS_2 layers *2D Mater.* **2** 035006

[27]   Dimitrievska M, Boero F, Litvinchuk A P, Delsante S, Borzone G, Perez-Rodriguez A and Izquierdo-Roca V 2017 Structural Polymorphism in "Kesterite" Cu_2ZnSnS_4: Raman Spectroscopy and First-Principles Calculations Analysis *Inorg. Chem.* **56** 3467–74

[28]   Pangilinan G, Sooryakumar R and Misiewicz J 1991 Raman activity of Zn_3P_2 *Phys. Rev. B* **44** 2582–8

[29]   Hanuza J, Lemiec A and Misiewicz J 1998 Molecular model of lattice vibrations in Zn_3P_2 *Vibrational Spectroscopy* **17** 93–103

[30]   Zhang X-J and Liu B-G 2016 Two-dimensional wide-band-gap II–V semiconductors with a dilated graphene-like structure *Semicond. Sci. Technol.* **31** 125002

[31]   Demers S and van de Walle A 2012 Intrinsic defects and dopability of zinc phosphide *Phys. Rev. B* **85** 195208

[32]   Yin W-J and Yan Y 2013 The electronic properties of point defects in earth-abundant photovoltaic material Zn_3P_2: A hybrid functional method study *Journal of Applied Physics* **113** 013708

[33]   Dzade N Y 2020 Unravelling the early oxidation mechanism of zinc phosphide (Zn_3P_2) surfaces by adsorbed oxygen and water: a first-principles DFT-D3 investigation *Phys. Chem. Chem. Phys.* **22** 1444–56

[34]   Dzade N Y 2020 First-Principles Insights into the Interface Chemistry between 4-Aminothiophenol and Zinc Phosphide (Zn_3P_2) Nanoparticles *ACS Omega* **5** 1025–32

[35]   Ghasemi M, Stutz E, Escobar Steinvall S, Zamani M and Fontcuberta i Morral A 2019 Thermodynamic re-assessment of the Zn–P binary system *Materialia* **6** 100301

[36]   Ceperley D M and Alder B J 1980 Ground State of the Electron Gas by a Stochastic Method *Phys. Rev. Lett.* **45** 566–9

[37]   Perdew J P and Zunger A 1981 Self-interaction correction to density-functional approximations for many-electron systems *Phys. Rev. B* **23** 5048–79

[38]   Clark S J, Segall M D, Pickard C J, Hasnip P J, Probert M I J, Refson K and Payne M C 2005 First principles methods using CASTEP *Zeitschrift fur Kristallographie* **220** 567–70

[39]   Aroyo M I, Perez-Mato J M, Orobengoa D, Tasci E, De La Flor G and Kirov A 2011 Crystallography online: Bilbao crystallographic server *Bulgarian Chemical Communications* **43** 183–97

[40]   Aroyo M I, Perez-Mato J M, Capillas C, Kroumova E, Ivantchev S, Madariaga G, Kirov A and Wondratschek H 2006 Bilbao Crystallographic Server: I. Databases and crystallographic computing programs *Zeitschrift für Kristallographie - Crystalline Materials* **221** 15–27

[41]   Aroyo M I, Kirov A, Capillas C, Perez-Mato J M and Wondratschek H 2006 Bilbao Crystallographic Server. II. Representations of crystallographic point groups and space groups *Acta Cryst A* **62** 115–28

[42]   Escobar Steinvall S, Ghisalberti L, Zamani R R, Tappy N, Hage F S, Stutz E, Zamani M, Paul R, Leran J-B, Ramasse Q M, Carter W C and Fontcuberta i Morral A 2020 Heterotwin Zn_3P_2 superlattice nanowires: the role of indium insertion in the superlattice formation mechanism and their optical properties *arXiv:2009.01533 [cond-mat]*

[43]   He J, Hummer K and Franchini C 2014 Stacking effects on the electronic and optical properties of bilayer transition metal dichalcogenides MoS_2, $MoSe_2$, WS_2, and WSe_2 *Phys. Rev. B* **89** 075409

[44]   Menéndez J and Cardona M 1985 Interference effects: A key to understanding forbidden Raman scattering by LO phonons in GaAs *Phys. Rev. B* **31** 3696–704

[45]   Amaduzzi F, Alarcón-Lladó E, Hautmann H, Tanta R, Matteini F, Tütüncüoğlu G, Vosch T, Nyg\aard J, Jespersen T, Uccelli E and Morral A F i 2016 Tuning the response of non-allowed Raman modes in GaAs nanowires *J. Phys. D: Appl. Phys.* **49** 095103

[46]   Poliani E, Wagner M R, Vierck A, Herziger F, Nenstiel C, Gannott F, Schweiger M, Fritze S, Dadgar A, Zaumseil J, Krost A, Hoffmann A and Maultzsch J 2017 Breakdown of Far-Field Raman Selection Rules by Light–Plasmon Coupling Demonstrated by Tip-Enhanced Raman Scattering *J. Phys. Chem. Lett.* **8** 5462–71

[47]   Takase M, Ajiki H, Mizumoto Y, Komeda K, Nara M, Nabika H, Yasuda S, Ishihara H and Murakoshi K 2013 Selection-rule breakdown in plasmon-induced electronic excitation of an isolated single-walled carbon nanotube *Nature Photonics* **7** 550–4

[48]   Ketterer B, Uccelli E and Morral A F i 2012 Mobility and carrier density in p-type GaAs nanowires measured by transmission Raman spectroscopy *Nanoscale* **4** 1789–93

[49]   Litvinchuk A P and Valakh M Y 2020 Raman and infrared phonons in tetragonal ZnP_2 and CdP_2 crystals: a density functional study *J. Phys.: Condens. Matter* **32** 445401

[50]   Dimitrievska M, Fairbrother A, Fontané X, Jawhari T, Izquierdo-Roca V, Saucedo E and Pérez-Rodríguez A 2014 Multiwavelength excitation Raman scattering study of polycrystalline kesterite Cu_2ZnSnS_4 thin films *Appl. Phys. Lett.* **104** 021901